Hydrodynamic Coupling Melts Acoustically Levitated Crystalline Rafts

Brady Wu,[1, 2, *] Bryan VanSaders,[2] Melody X. Lim,[1, 2, †] and Heinrich M. Jaeger[1, 2]

[1]*Department of Physics, University of Chicago*
[2]*James Franck Institute, University of Chicago*

The acoustic levitation of small particles provides a versatile platform to investigate the collective dynamical properties of self-assembled many-body systems in the presence of hydrodynamic coupling. However, acoustic scattering forces can only generate attractive interactions at close range in the levitation plane, limiting self-assembly to rafts where particles come into direct, dissipative, contact. Here, we overcome this limitation by using particles small enough that the viscosity of air establishes a repulsive streaming flow at close range. By tuning the size of particles relative to the characteristic length scale of the viscous flow, we control the interplay between attractive and repulsive forces. In this novel granular raft, particles form an open lattice with tunable spacing. Hydrodynamic coupling between particles gives rise to spontaneous excitations in the lattice, in turn driving intermittent particle rearrangements. Under the action of these fluctuations, the raft transitions from a predominantly quiescent, crystalline structure, to a two-dimensional liquid-like state. We show that this transition is characterized by dynamic heterogeneity and intermittency, as well as cooperative particle movements, that produce an effectively 'cageless' crystal. These findings shed light on fluid-coupling driven excitations that are difficult to isolate and control in many other hydrodynamic systems.

Acoustic levitation has been widely used as a contact-free technique to manipulate particles and direct particle self-assembly [1–9]. It has also been used to study the collective properties of many body systems [10–13]. Within the nodal plane of an acoustic cavity, scattered sound waves establish tunable attractions between particles [14], aggregating them together into a close-packed monolayer raft. Sub-millimeter granular particles are too large for thermal noise to drive their dynamics. However, other athermal fluctuations can be introduced by slightly detuning the cavity excitation away from its resonant frequency, which results in vertical oscillations [10, 15, 16] or spontaneous rotation of the entire raft [11].

Such fluctuations are a manifestation of hydrodynamic instabilities (HIs), where the configuration of particles moving relative to a surrounding fluid evolves unpredictably due to hydrodynamic coupling. HI-induced excitations in many-body systems can exhibit complex correlations that control collective properties, in contrast to uncorrelated thermal fluctuations. In the above-mentioned prior work, the fluctuations emerged from feedback between a moving object and the acoustic cavity mode, an instability found already for a single levitated particle [15, 16]. A more subtle instability can arise from the hydrodynamic coupling among multiple particles. For example, such HIs can occur among neighboring particles settling in a fluid [17, 18], and it has been associated with the chaotic trajectories of small numbers of weakly interacting steel spheres in an oscillating glycerol bath [19]. Acoustic levitation has proven to be a powerful technique to observe multiple forms of HIs in systems of hundreds of particles evolving over long time scales. However, strongly dissipative frictional particle contacts in prior studies [10, 11] masked the presence of HIs arising from the relative motion of particles.

Here, we overcome this limitation by levitating particles small enough that a viscosity-driven repulsive streaming flow can have an appreciable effect on the structure of the particle assemblies. When the levitated particles are comparable in size to the extent of the streaming flows, the repulsive hydrodynamic forces can counteract attractive scattering forces at close range. By tuning the particle size, and by extension, the relative strengths of attraction and repulsion, we are able to vary the stable distance between pairs of levitated particles from contact to a particle diameter apart (Fig 1 **b-f**). Underdamped and contactless, the particles can be now be driven by excitations arising from their hydrodynamic coupling.

We find that the sound energy density of the cavity determines the magnitude of HI-driven excitations, controlling the transition from a quiescent crystal-like state to a highly diffusive liquid-like state. As a result of fluid-induced spatio-temporal correlations, this transition is mediated by intermittent, avalanche-like dynamics where a single displacement event can trigger system wide rearrangements, a clear distinction from the spatially homogeneous thermal melting transition [20, 21]. Fundamentally, the avalanche-like excitation arises as a consequence of the correlated motion between neighboring particles starting from the ballistic time scale, which produces an effectively 'cageless' crystal over long time scales. In contrast to similar phenomenon in kinetically trapped systems [22], avalanche-like events in levitated rafts do not relax by the descent of a rough configurational landscape and can continue indefinitely.

Our experimental setup is illustrated in Fig 1 **a**. A resonating acoustic cavity is driven on one side by an ultrasonic transducer, which is bolted to an aluminum horn to maximize power output. The resonant frequency
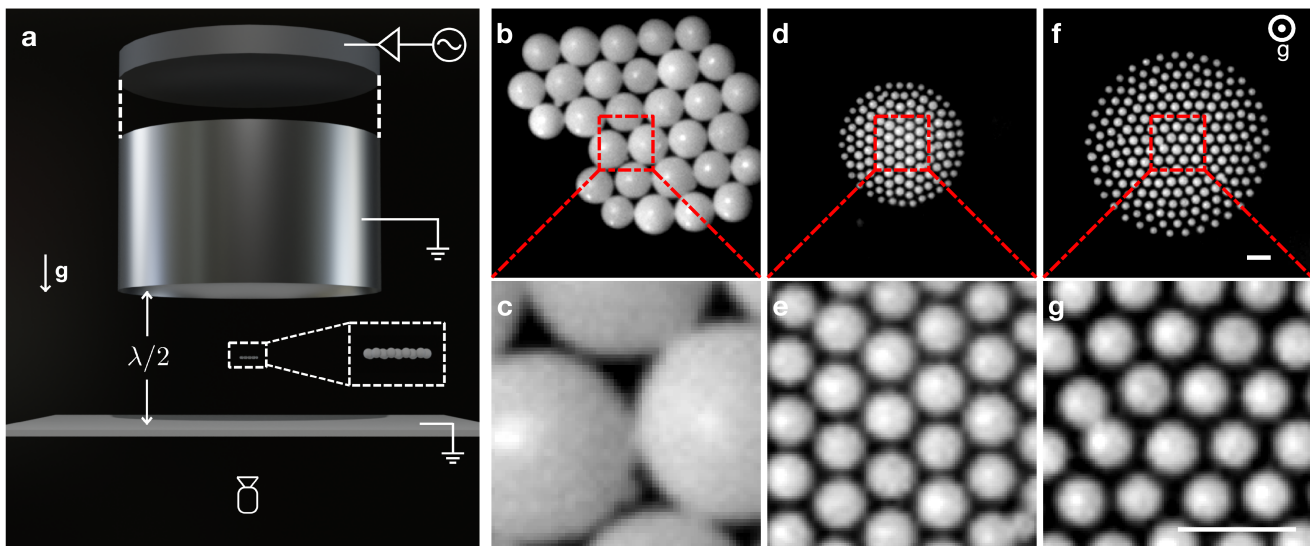
FIG. 1. **Acoustically levitated particles with tunable interactions. a**, Schematic of the experimental setup. The transducer consists of an aluminum resonating horn (bottom) and a piezoelectric driving element (top). Ultrasonic standing waves (of wavelength λ) form between the transducer and reflector. Particles are levitated at the pressure nodal plane. A high-speed video camera is used to obtain the bottom view. **b-g**, Images of levitated particle clusters (top) and zoomed-in (bottom) views of interparticle spacing. Average particle diameter and frequency are **b** $D = 180\mu m$, $f = 34.7$ kHz ($\lambda = 9.55$ mm), **d** $D = 40\mu m$, $f = 64.3$ kHz ($\lambda = 5.23$ mm), and **f** $D = 40\mu m$, $f = 34.7$ kHz ($\lambda = 9.55$ mm). Scale bars correspond to $100\ \mu m$.

f_0 of the coupled transducer and horn is 34,870Hz, with an associated free space wavelength $\lambda = c/f_0 \simeq 9.8mm$, where c is the speed of sound in air (Supplementary Section 1). Here, we use polyethylene particles of diameter $D = 30 - 60\mu m$ (Supplementary Section 2 and 3), such that the setup operates deep in the Rayleigh scattering regime ($\lambda > D$). Unlike larger levitated objects [10, 15, 16], these particles compose a negligible volume fraction of the resonating cavity. As a result, changing the driving frequency or amplitude adjusts the energy density of the acoustic cavity without triggering spontaneous vertical oscillations of individual particles. Confined by single-scattering forces (i.e. primary forces) [23, 24], particles levitate at the pressure nodal plane, and are imaged from below using a high-speed camera (Fig 1 **b-f**).

Tunable attractive and repulsive interactions. At low energy density in the cavity, particles levitate in stationary configurations and do not fluctuate. The equilibrium distances between particles are determined by the competition of attractive and repulsive interparticle forces. Attractive forces arise from the scattering of sound between particles. These long-range secondary radiation forces are anisotropic, with attraction for particle configurations in the nodal plane and repulsion out of the plane [14] (Fig. 2 **a**). The magnitude of in-plane attraction as a function of distance scales as

$$F_{rad}(r) \propto -\frac{E_0 D^6}{r^4 \lambda^3}, \qquad (1)$$

where $E_0 \equiv \rho_0 V_0^2/2$ is the energy density of the acoustic field in air with maximum velocity V_0, density ρ_0, wavelength λ, and r is the center-to-center distance between particles of diameter D [14].

Interparticle repulsion arises from a viscosity (ν) effect, and is not captured by the above scattering analysis. Near particle surfaces a viscous boundary layer of characteristic thickness $\delta_\nu = \sqrt{\nu/\pi f}$ forms, over which the velocity of air relative to the particle surface decays to zero. Within the boundary layer, acoustic energy is coupled to steady, short-ranged flows. For particle sizes much larger than δ_ν, the influence of this boundary layer is negligible; however, for $D \approx \delta_\nu$, the time-averaged, non-linear microstreaming flows that develop within the viscous boundary layer surrounding the particle become significant. These flows form two toroidal vortices around the sphere, aligned with the axis of the exciting wave [26]. Flow in the levitation plane near the particle surface is outward, opposing attraction from the radiation force (Fig. 2 **b**). The magnitude of this microstreaming-induced repulsion depends primarily on δ_ν, which is similar for particles of all sizes at the same driving frequency f. Therefore, as particle size decreases, the relative magnitude of the viscous correction to the short-ranged interaction grows. As viscous forces are nearly constant, while F_{rad} scales with D^6 (Eq. 1), interparticle separation increases with smaller particle size.

To analyze this quantitatively, we calculate interparticle forces using the Lattice Boltzmann method (LBM), a discretized direct fluid simulation technique (see Meth-
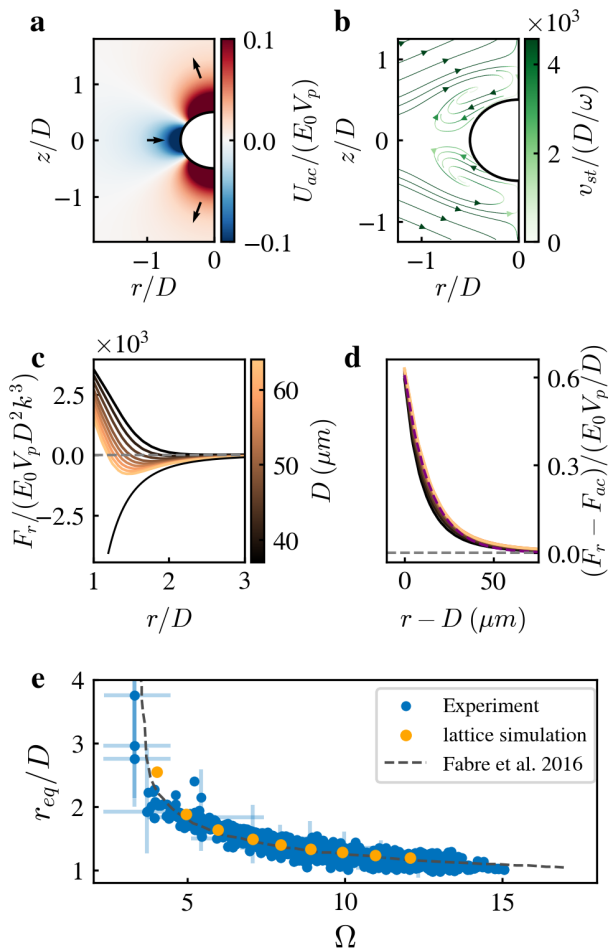
FIG. 2. **Short-ranged repulsive interactions from viscous effects. a**, The acoustic scattering potential, U_{ac}, in the x-z plane. The interaction is attractive in the equatorial while repulsive in the polar direction. The white circle represents the particle. **b**, Time-averaged microstreaming flow of magnitude v_{st} around a sphere, as obtained by Lane [25]. The direction of flow-induced forces in the levitation plane are opposite to that in **a**. **c**, The magnitude of force in the equatorial direction F_r as a function of radial distance r for various particle diameter, as calculated with a lattice fluid simulation. The black curve represents the force from the scattering expansion following [14]. **d**, The magnitude of the microstreaming repulsive interaction, approximated by subtracting the scattering expansion from the lattice fluid force traces in **c**. The purple dashed line represents an exponential fit, $a * exp(-(r - D)/\kappa)$; $\kappa \approx 14\mu m$. **e**, The equilibrium distance r_{eq}/D between a particle pair as a function of Stokes number Ω. Blue errorbars represent the uncertainties for selected data points (Supplementary Section 2).

ods). Figure 2 **c** shows the force experienced between pairs of variously-sized particles, scaled by the non-dimensional prefactor of the scattering expansion pair interaction. For $r/D > 2$, pair forces are attractive for most sizes, and larger particles more closely follow the

form of the scattering expansion (black curve). We estimate the form of the viscous repulsive interaction by subtracting the scattering expansion from the net force, yielding the data in Fig. 2 **d**. As expected, the decay of viscous repulsion from the particle surface is nearly independent of diameter, and exponential over the thickness of the viscous layer δ_ν.

The competition between scattering and viscous forces produces stable in-plane equilibrium separations which are controlled by the Stokes number $\Omega = 2\pi f R^2/\nu$ [27]. Figure 2 **e** compares the numerical results for the equilibrium, in-plane center-to-center particle distance r_{eq} from Fabre et al. [27] with our LBM simulations and experimental observations, showing close agreement. Importantly, we find no significant difference in r_{eq} when comparing isolated particle pairs with pairs of neighboring particles inside large rafts (Supplementary Section 4). These results are consistent with prior investigations of centimeter-scale spherical particles in a confined, oscillating viscous liquid [19, 28–30].

Order-to-disorder transition. In the following we focus on levitated rafts with $\Omega \approx 6$, and induce stochastic particle dynamics by increasing the applied oscillation amplitude, parameterized here by the acoustic pressure in the cavity, P_{acous}. The intensity of acoustic driving controls the transition from a quiescent crystal-like state (Fig. 3 **a**, **i**) with well-defined equilibrium interparticle spacings, to a liquid-like state (Fig. 3 **a**, **ii**) with rapidly fluctuating particle positions and associated kinetic energy (Fig. 3 **b** and Supplementary Video 1). We note that all motion in this liquid state occurs within the levitation plane and does not involve excursions into the vertical direction (Supplementary Video 2). The particles' velocity distribution is isotropic and well-described as a traditional granular gas (Supplementary Section 5). The interaction of the raft with the acoustic field in the cavity produces a reduced local energy density at the edge of the raft, thus producing distinctive rings of particles that rarely leave their respective annuli (Supplementary Section 6).

To quantify how disorder emerges in the crystal-like state as P_{acous} is increased, we calculate the spatially and long-time averaged bond order parameter $\Phi_6 = \langle\frac{1}{N_{nn}}\sum_{nn} e^{i6\theta_i}\rangle_N$, where θ_i is the angle between the bond and an arbitrary axis, nn denotes nearest neighbor, N_{nn} is the number of neighbor particles, and the average is over all particles N [20, 21]. We find that Φ_6 monotonically decreases with increasing P_{acous} (Fig. 3 **c**). At first glance this is surprising, given that the strength of interparticle, in-plane attractive forces increases with energy density in the cavity and thus P_{acous} (see Eq. 1 and Fig. 2 **c**). Stronger interparticle binding promotes crystalline order; however, we find that the acoustic energy density increases the strength of HI-driven perturbations more rapidly, allowing us to to observe an order-to-disorder transition.
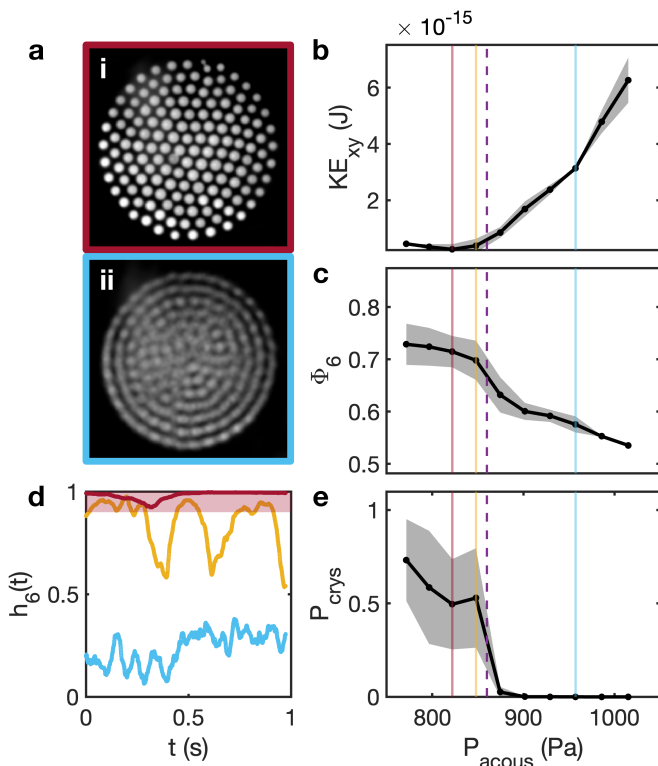
FIG. 3. **Acoustic energy density controls crystal-liquid transition. a**, Time averaged images of crystal-like (**i**) and liquid-like (**ii**) states over $167ms$ at $P_{acous} = 822\,Pa$ and $P_{acous} = 957\,Pa$. **b-c**, The average kinetic energy in xy direction KE_{xy}, and the bond order parameter ϕ_6 as a function of acoustic pressure, P_{acous}. **d**, The bond correlation function $h_6(t) = \langle \phi_6(t - \Delta t) \cdot \phi_6(t) \rangle$ for crystal (maroon), liquid (blue), and intermittent dynamics (orange). $\Delta t = 10ms$. We define P_{crys} as the probability of $h_6 > 0.9$ (the shaded region). **e**, The probability of crystal-like state, P_{crys}, as a function of P_{acous}.

We observe that this order-to-disorder transition is characterized by sudden, avalanche-like rearrangements (Fig. 4 **a**). To quantify these excursions, we calculate a spatially averaged, local order correlation function, $h_6(t, \Delta t) = \langle \Phi_6(t - \Delta t) \cdot \Phi_6(t)^* \rangle_N$, which measures how much local 6-fold orientational order (Φ_6) changed over a short time interval Δt before time t, averaged over N particles. $h_6 = 1$ indicates no change in ordering, while h_6 close to zero corresponds to the decorrelation of local bond order. A characteristic decorrelation time $\Delta t = 10ms$ was chosen for the liquid state, but the behavior of h_6 shown here is not sensitive to choices of Δt from 5 to 100ms.

Figure 3 **d** shows the evolution of h_6 for three representative cases. Rafts exhibit intermittent dynamics (orange), where $h_6(t)$ switches between low and high values at random intervals, indicating that the raft behaves as a crystal-like state with stochastic bursts of liquid-like rearrangements. The quiescent, crystal-like state has a wide range of lifetime, from fractions of a second to a few sec-

onds, but will eventually be interrupted by a liquid-like excitation. In the crystal-like state the particle displacements are smaller than a lattice spacing, and account for all decorrelations $h_6 > 0.9$ (red shaded band). For example, the dip in h_6 for the red trace around 0.3s is due to phonon motion in an otherwise stationary crystal. Finally, at large P_{acous}, the raft enters a liquid-like state, with $h_6 < 0.5$. Defining the probability P_{crys} of finding the raft in the crystal-like state as the fraction of time that $h_6 > 0.9$, we observe a sharp drop around $P_{acous}^* \approx 860 Pa = 1.1 P_{acous}^{min}$ (P_{acous}^* is the purple dashed line in Fig. 3 **b,c,e**, $P_{acous}^{min} = 780$Pa is the minimum pressure at which rafts can be stably levitated), signaling the transition from the stochastically interrupted crystal-like state, to a consistently liquid-like state.

Intermittent dynamics from cooperative motion. We now look in more detail at the structural rearrangements that are produced by HIs inside a raft. Intermittent excursions into the liquid-like state can be identified by pulses in the kinetic energy per particle (Fig. 4 **a** inset), where each pulse is an intense, avalanche-like excitation. Between such events, the system settles into an idle, highly ordered crystal state (Supplementary Video 3). These excited and quiescent states exist for similar amounts of time and typically each last for a fraction of a second. At the onset of an event (Fig. 4 **a**), the kinetic energy increases smoothly at about the same rate as it decays by viscous damping of individual particle motions in air. This similarity in the rates of energy increase and decrease implies that the energy is injected locally via viscous streaming flows, on a per particle basis, rather than through a sudden external, boundary-coupled perturbation (e.g., via an air current).

To better understand these intermittent excursions, we next examine the per-particle dynamics of a representative event. We define a reference time t_0, immediately before the onset of the event for comparison with later times, t. In Fig. 4 **b**, arrows indicate particle displacements from t_0 to t. Particles positions at time t are shown and colored according to their kinetic energy. An event typically starts with chain-like rearrangements at the raft edge, the locations of which are correlated with defects that delineate the interface between the raft's core and its outer layers, as shown in Fig. 4 **a**, **i–ii** (Supplementary section 7) [31]. Particle motion creates more defects which propagate through the entire extent of the raft (Supplementary section 8), inducing an avalanche-like burst of collective rearrangement that persists until the kinetic energy is dissipated and the system attains some stable configuration. We note that there is significant spatial heterogeneity in the particle rearrangements during an event, with the most mobile particles tending to collectively move in a linear path through the raft, similar to what has been observed in glassy supercooled liquids [32–34].

A crucial distinction between our levitated rafts and
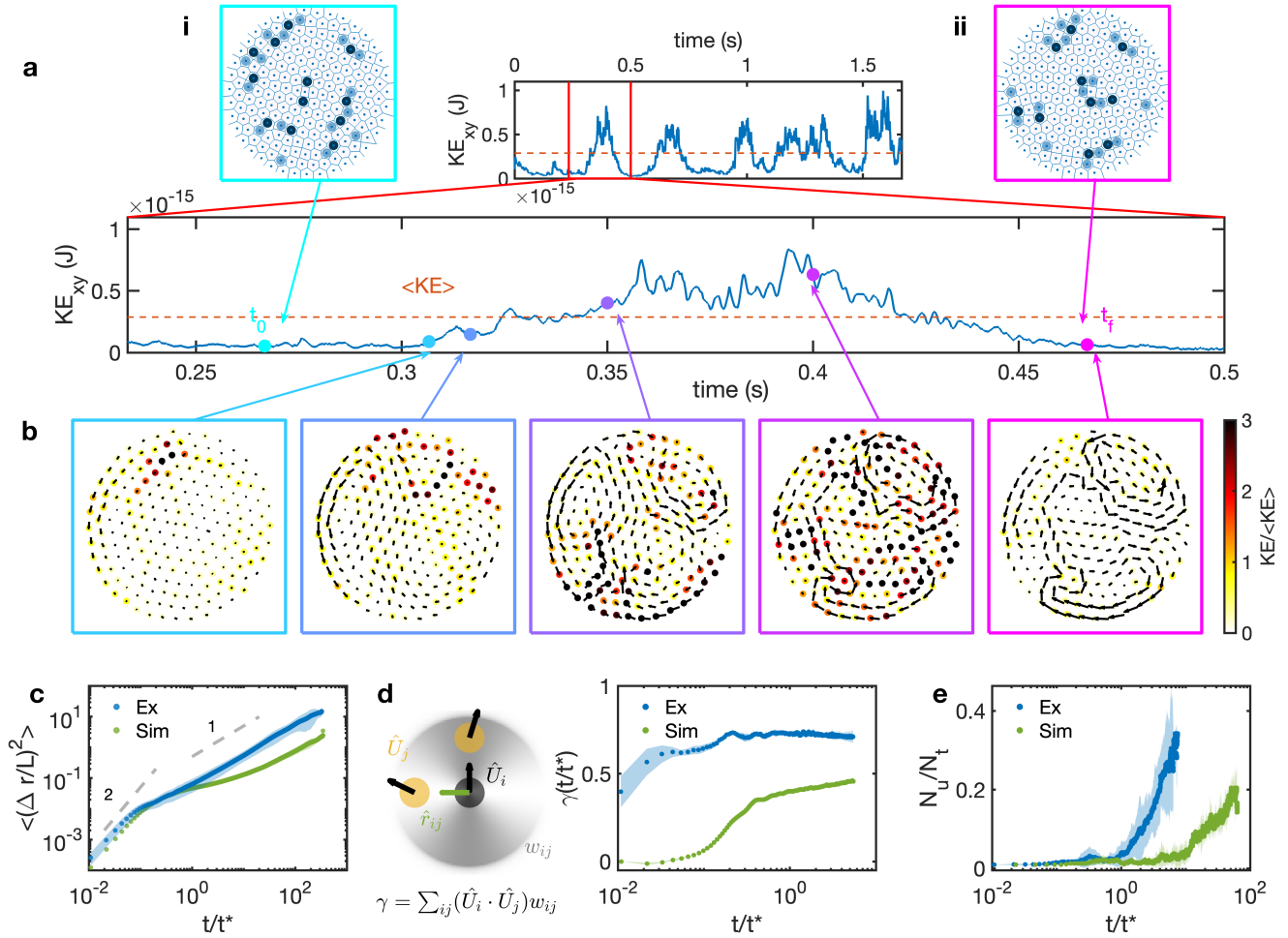
FIG. 4. **Cooperative uncaging drives intermittent dynamics. a,** The kinetic energy per particle within a raft during an avalanche. The inset exhibits several avalanches within a span of 1.5s. The particular avalanche in the main panel of **a** is boxed in red. The average kinetic energy per particle over 10s is plotted in orange dashed lines. The marked points correspond to the snapshots in **b**. **i-ii,** The voronoi construction of the cluster configuration at t_0 and t_f. Light and dark blue represents the 5 and 7 particles defect. **b,** A time sequence of a raft displaying an intermittent avalanche event. Arrows denote the displacement field from time t_0 before the event, as indicated in **a**. Particles are colored with their current values of $KE/\langle KE \rangle$. **c,** Normalized mean square displacement $\langle(\Delta r/L)^2\rangle$ as a function of t/t^* for both the experiment and MD simulation. L denotes the lattice spacing, and $t^* = L/\langle v \rangle$. **d,** $\langle \gamma \rangle$ as a function of the normalized time. The schematic shows the definition of γ. $w_{ij} = (\hat{U}_i \cdot \hat{r}_{ij})^2$ is the angular weighting function and depicted with the shaded area; the directions parallel to the particle motion are weighted more heavily. **e,** The fraction of uncaged particles in a raft, N_u/N_t, as a function of t/t^*. N_u and N_t are the uncaged and total particle number, respectively. A particle is considered uncaged if the displacement from time t_0 is greater than $\langle v \rangle t^*$. The shaded area represents standard deviation from 10 independent avalanche events in the same raft.

supercooled liquids is in the pre- and post- event configurations. Glassy systems drive avalanche events by descending a rough free-energy landscape, a process that starts with large displacements localized near 'hot spots', but eventually arrests as the ground state is approached. In contrast, levitated rafts undergo intermittent avalanche-like events indefinitely, and crystal-like configurations before and after events are not distinctly different (Fig. 4 **a**, **i**–**ii** and Supplementary section 9). Furthermore, avalanche-like events in levitated rafts are not localized and eventually involve the entire system.

In order to illuminate the nonequilibrium nature of

these hydrodynamically driven raft rearrangements, we compare our experimental results with predictions based on a thermal ensemble of particles. To this end, we plot the mean square displacement (MSD) for both the experiment and a molecular dynamics simulation (Supplementary section 10) with pair-wise interactions (Fig. 4 **c**). To properly compare the data, we non-dimensionalize distances by the lattice spacing L, and times by the time taken for a particle to ballistically travel a distance of one lattice spacing $t^* = L/\langle v \rangle_{N,t}$. For particles in a thermal bath and with $k_B T/V_B = 0.04$ (the case most analogous to our experiments, see Supplementary section 10

for details), where V_B is the binding energy, the MSD traces exhibit ballistic behavior for $t << t^*$, caging for $t \approx t^*$, and diffusive motion for $t >> t^*$ [35]. In contrast, the experimental MSD does not exhibit any caging behavior. Instead, it transitions directly from ballistic to diffusive behavior around $t \approx 0.1t^*$. This behavior is reminiscent to that of a liquid or gas, without lattice ordering to induce intermediate-time caging. Notably, although the experiment has an effective temperature $\langle KE_{x,y} \rangle / V_B = 8 \times 10^{-4}$, nearly 50 times lower than the simulation counterpart, the experimental particles are more mobile due to the presence of intermittent avalanches.

To further examine this exotic behavior, we define the velocity-direction correlation parameter

$$\gamma(t) = \sum_{ij} (\hat{U}_i(t) \cdot \hat{U}_j(t)) w_{ij}(t), \qquad (2)$$

where $\hat{U}_i$ and $\hat{U}_j$ are the unit vectors of displacement for neighboring particles i and j, and $\hat{r}_{ij}$ is the displacement vector between particles. In addition, we define a weight density $w_{ij}(t) = (\hat{U}_i(t) \cdot \hat{r}_{ij}(t))^2$, indicated by the shading in the schematic of Fig. 4 **d**, such that directions parallel to the velocity of the particle are weighted more than those perpendicular. Our results are plotted in Fig. 4 **d**, and show that the levitated particles display highly correlated motions even at short times. In contrast, the motions of particles in the simulation are uncorrelated, and only begin to correlate after the ballistic regime $t > 0.1t^*$. Fundamentally, this contrast highlights the difference between excitation induced by HIs and by thermal fluctuation. Excitations from HIs display a high degree of spatio-temporal correlation and depend on the configuration of nearby particles.

We show that this spatio-temporal correlation results in the lack of particle caging by measuring the number of particles that escape their caging neighborhood over time. Here, particles are considered to have escaped their cage if they traversed at least one lattice spacing relative to t_0. Our results are plotted in Fig. 4 **e**, and show that the levitated particles begin to uncage at $t \approx t^*$, which is the time particles will take to cross a distance L if their motion is ballistic. In contrast, the simulated system only starts to uncage for $t \approx 10t^*$, which is when the particle motion becomes diffusive. This distinction shows how the correlated motions make the levitated crystal susceptible to perturbations, as a single uncaging event is amplified into a system-spanning event by the tendency of interparticle HIs to correlate particle motions.

Taken together, our results establish acoustically-levitated rafts as a potent platform for investigating how hydrodynamic coupling can spontaneously excite a many-body system. By tuning the relative strength of attractive scattering interactions and repulsive microstreaming flows, particle configurations exhibit hydro-

dynamic instabilities that scale in magnitude with applied acoustic pressure more quickly than any stabilizing acoustic binding. As a consequence, increasing acoustic pressure drives rafts through an order-to-disorder transition. Unlike the melting of a two-dimensional crystal in thermal equilibrium, this order-to-disorder transition occurs through intermittent periods of liquid-like behavior that eventually merge into a two-dimensional fluid-like steady state. These intermittent, spatially correlated events reveal that hydrodynamic-instability-driven excitations are not equivalent to their thermal counterparts, in line with recent results for active systems that demonstrate the central role of statistical decorrelation between driven and fluctuating degrees of freedom in order to recover thermal-like behavior [36]. Levitated rafts may also serve as a highly suitable system to explore experimentally the link between spatially-varying dissipation and dynamic transitions, as seen in simulations of active matter [37, 38]. Finally, our results provide valuable insight into the limits of acoustic many-body control, elucidating a key instability mechanism that affects the precision of acoustic manipulation at small scales.

EXPERIMENTAL SETUP AND METHOD

Experiment

Our acoustic cavity is driven on one side by a commercial ultrasonic transducer. An aluminum horn is bolted onto the transducer to amplify the acoustic power generation. The bottom of the metallic horn has a concave radius of curvature $R = 50mm$ and was painted black to minimize light reflection. The concave geometry weakly confines the particles at the center of the trap. A commercial heat tape, regulated with a PID temperature controller, is wrapped around the horn and maintains the transducer at $35 \pm 0.5°C$ for experimental repeatability. The transducer is driven by applying a sinusoidal wave of peak-to-peak voltage V_{pp} (60-200V) and frequency close to the resonance frequency of the horn, $f_0 = 34.85kHz$; this signal is generated from a function generator and amplified by a high-voltage amplifier (A-301 HV amplifier, AA Lab Systems). The reflector consists of an acrylic plate (bottom) and an ITO-coated glass slide (top). To reduce the effect of tribocharging, both the horn and reflector were grounded. The distance between the edge of the horn and the reflector can be adjusted with a translation stage to $\lambda/2 = 4.9mm$. In order to minimize the effect of air currents, the entire setup was enclosed within an acrylic box with dimensions much larger than the levitation region ($l \times w \times h = 61 \times 30 \times 46 \times cm^3$).

We used polyethylene spherical particles (Cospheric, material density $\rho = 1000kgm^{-3}$, diameter d=30-60 μm, see Supplementary Section 2 and 3 for particle size distribution). The particles are stored, and all experiments are performed within a humidity and temperature-controlled laboratory environment (45-50 % relative humidity,22-24°C).

Before and after each experiment, the setup was cleaned with de-ionized water and dried with compressed air. For each experiment, the particles were added to the cavity with a tweezer. Videos are recorded with a high-speed camera (Vision Research Phantom T1340) at 3000 frames per second. The acoustic pressure generated is measured with Xarion optical microphone (Eta100 Ultra).

Lattice Boltzmann Simulation

The Lattice Boltzmann method (LBM) was used to perform simulations of particles interacting through acoustically-mediated forces. This method captures the full extent of the fluid-structure interactions, naturally including the effects of viscous dissipation and momentum transfer due to multiple scattering events. LBM simulations of the acoustic cavity were performed within the `waLBerla` framework [39]. A single relaxation time scheme with a viscosity matching that of air was used [40]. Particles were simulated in periodic domains to avoid spurious boundary reflections. A spatially-homogeneous background force field was used to oscillate the background fluid. The `PE` functionality of the `waLBerla` framework was used to simulate the interaction of particles with the acoustic field [41]. Hydrodynamic forces between the particles and fluid were handled with the partially-saturated cells method [42]. A local cell size of $D/15$, where D is the particle diameter, was sufficiently high lattice resolution for accurate force calculations.

* email: bwu34@uchicago.edu

† Present address: Laboratory of Solid State and Atomic Physics, Cornell University

[1] A. Marzo, S. A. Seah, B. W. Drinkwater, D. R. Sahoo, B. Long, and S. Subramanian, Holographic acoustic elements for manipulation of levitated objects, Nature Communications **6**, 8661 (2015).

[2] G. Memoli, M. Caleap, M. Asakawa, D. R. Sahoo, B. W. Drinkwater, and S. Subramanian, Metamaterial bricks and quantization of meta-surfaces, Nature Communications **8**, 14608 (2017).

[3] D. Foresti, M. Nabavi, M. Klingauf, A. Ferrari, and D. Poulikakos, Acoustophoretic contactless transport and handling of matter in air, Proceedings of the National Academy of Sciences **110**, 12549 (2013).

[4] T. M. Llewellyn-Jones, B. W. Drinkwater, and R. S. Trask, 3D printed components with ultrasonically arranged microscale structure, Smart Materials and Structures **25**, 02LT01 (2016).

[5] K. Melde, A. G. Mark, T. Qiu, and P. Fischer, Holograms for acoustics, Nature **537**, 518 (2016).

[6] D. Ahmed, A. Ozcelik, N. Bojanala, N. Nama, A. Upadhyay, Y. Chen, W. Hanna-Rose, and T. J. Huang, Rotational manipulation of single cells and organisms using acoustic waves, Nature Communications **7**, 11085 (2016).

[7] Q. Shi, W. Di, D. Dong, L. W. Yap, L. Li, D. Zang, and W. Cheng, A General Approach to Free-Standing Nanoassemblies via Acoustic Levitation Self-Assembly, ACS Nano **13**, 5243 (2019).

[8] Z. Chen, D. Zang, L. Zhao, M. Qu, X. Li, X. Li, L. Li, and X. Geng, Liquid Marble Coalescence and Triggered Microreaction Driven by Acoustic Levitation, Langmuir **33**, 6232 (2017).

[9] S. Tsujino and T. Tomizaki, Ultrasonic acoustic levitation for fast frame rate X-ray protein crystallography at room temperature, Scientific Reports **6**, 25558 (2016).

[10] M. X. Lim, A. Souslov, V. Vitelli, and H. M. Jaeger, Cluster formation by acoustic forces and active fluctuations in levitated granular matter, Nature Physics **15**, 460 (2019).

[11] M. X. Lim, B. VanSaders, A. Souslov, and H. M. Jaeger, Mechanical Properties of Acoustically Levitated Granular Rafts, Physical Review X **12**, 021017 (2022).

[12] R.-Y. Dong, W. Wang, and S. Granick, Colloidal Flatlands Confronted with Urge for the Third Dimension, ACS Nano **13**, 9442 (2019).

[13] M. A. Abdelaziz, J. A. Dĩaz A., J.-L. Aider, D. J. Pine, D. G. Grier, and M. Hoyos, Ultrasonic chaining of emulsion droplets, Physical Review Research **3**, 043157 (2021).

[14] G. T. Silva and H. Bruus, Acoustic interaction forces between small particles in an ideal fluid, Physical Review E **90**, 063007 (2014).

[15] J. Rudnick and M. Barmatz, Oscillational instabilities in single-mode acoustic levitators, Acoustical Society of America Journal **87**, 81 (1990).

[16] M. A. B. Andrade, S. Polychronopoulos, G. Memoli, and A. Marzo, Experimental investigation of the particle oscillation instability in a single-axis acoustic levitator, AIP Advances **9**, 035020 (2019).

[17] I. M. Jãnosi, T. Tãl, D. E. Wolf, and J. A. C. Gallas, Chaotic particle dynamics in viscous flows: The three-particle Stokeslet problem, Physical Review E **56**, 2858 (1997).

[18] R. Chajwa, N. Menon, and S. Ramaswamy, Kepler Orbits in Pairs of Disks Settling in a Viscous Fluid, Physical Review Letters **122**, 224501 (2019).

[19] C. C. Thomas and J. P. Gollub, Structures and chaotic fluctuations of granular clusters in a vibrated fluid layer, Physical Review E **70**, 061305 (2004).

[20] K. Zahn and G. Maret, Dynamic Criteria for Melting in Two Dimensions, Physical Review Letters **85**, 3656 (2000).

[21] A. L. Thorneywork, J. L. Abbott, D. G. Aarts, and R. P. Dullens, Two-Dimensional Melting of Colloidal Hard Spheres, Physical Review Letters **118**, 158001 (2017).

[22] H. J. Hwang, R. A. Riggleman, and J. C. Crocker, Understanding soft glassy materials using an energy landscape approach, Nature Materials **15**, 1031 (2016).

[23] L. V. King, On the acoustic radiation pressure on spheres, Proceedings of the Royal Society of London. Series A - Mathematical and Physical Sciences **147**, 212 (1934).

[24] L. P. Gor'kov, On the Forces Acting on a Small Particle in an Acoustical Field in an Ideal Fluid, Soviet Physics Doklady **6**, 773 (1962).

[25] C. A. Lane, Acoustical streaming in the vicinity of a sphere, Journal of the Acoustical Society of America **27**, 1082 (1955).

[26] C. A. Lane, Acoustical Streaming in the Vicinity of a Sphere, The Journal of the Acoustical Society of America **27**, 1082 (1955).

[27] D. Fabre, J. Jalal, J. S. Leontini, and R. Manasseh, Acoustic streaming and the induced forces between two spheres, Journal of Fluid Mechanics **810**, 378 (2017).

[28] D. Klotsa, M. R. Swift, R. M. Bowley, and P. J. King, Chain formation of spheres in oscillatory fluid flows, Physical Review E **79**, 021302 (2009).

[29] G. A. Voth, B. Bigger, M. R. Buckley, W. Losert, M. P. Brenner, H. A. Stone, and J. P. Gollub, Ordered Clusters and Dynamical States of Particles in a Vibrated Fluid, Physical Review Letters **88**, 234301 (2002).

[30] F. Otto, E. K. Riegler, and G. A. Voth, Measurements of the steady streaming flow around oscillating spheres using three dimensional particle tracking velocimetry, Physics of Fluids **20**, 093304 (2008).

[31] M. Kong, B. Partoens, and F. M. Peeters, Topological defects and nonhomogeneous melting of large two-dimensional Coulomb clusters, Physical Review E **67**, 021608 (2003).

[32] A. Widmer-Cooper, P. Harrowell, and H. Fynewever, How Reproducible Are Dynamic Heterogeneities in a Supercooled Liquid?, Physical Review Letters **93**, 135701 (2004).

[33] A. S. Keys, A. R. Abate, S. C. Glotzer, and D. J. Durian, Measurement of growing dynamical length scales and prediction of the jamming transition in a granular material, Nature Physics **3**, 260 (2007).

[34] C. Reichhardt and C. J. Olson Reichhardt, Fluctuating Topological Defects in 2D Liquids: Heterogeneous Motion and Noise, Physical Review Letters **90**, 095504 (2003).

[35] E. R. Weeks and D. A. Weitz, Subdiffusion and the cage effect studied near the colloidal glass transition, Chemical Physics Strange Kinetics, **284**, 361 (2002).

[36] M. Han, M. Fruchart, C. Scheibner, S. Vaikuntanathan, J. J. de Pablo, and V. Vitelli, Fluctuating hydrodynamics of chiral active fluids, Nature Physics **17**, 1260 (2021).

[37] F. Cagnetta, F. Corberi, G. Gonnella, and A. Suma, Large Fluctuations and Dynamic Phase Transition in a System of Self-Propelled Particles, Physical Review Letters **119**, 158002 (2017).

[38] L. Tociu, Ã. Fodor, T. Nemoto, and S. Vaikuntanathan, How Dissipation Constrains Fluctuations in Nonequilibrium Liquids: Diffusion, Structure, and Biased Interactions, Physical Review X **9**, 041026 (2019).

[39] M. Bauer, S. Eibl, C. Godenschwager, N. Kohl, M. Kuron, C. Rettinger, F. Schornbaum, C. Schwarzmeier, D. Thönnes, H. Köstler, *et al.*, walberla: A block-structured high-performance framework for multiphysics simulations, Computers & Mathematics with Applications **81**, 478 (2021).

[40] D. Yu, R. Mei, L.-S. Luo, and W. Shyy, Viscous flow computations with the method of lattice boltzmann equation, Progress in Aerospace sciences **39**, 329 (2003).

[41] J. Götz, K. Iglberger, C. Feichtinger, S. Donath, and U. Rüde, Coupling multibody dynamics and computational fluid dynamics on 8192 processor cores, Parallel Computing **36**, 142 (2010).

[42] D. Owen, C. Leonardi, and Y. Feng, An efficient framework for fluid–structure interaction using the lattice boltzmann method and immersed moving boundaries, International Journal for Numerical Methods in Engineering **87**, 66 (2011).

Author contributions

B.W., B.V.S., and H.M.J. designed the study. M.X.L. designed the original experimental apparatus. B.W. modified the apparatus and performed the experiments. B.W. performed molecular dynamics simulations and analyzed the data. B.V.S. performed the lattice Boltzmann simulations and analyzed the data. All authors interpreted the results and and contributed to writing the manuscript.

Competing interests

The authors declare no competing interests.